Acta Materialia 211 (2021) 116863

Contents lists available at ScienceDirect

Acta Materialia

journal homepage: www.elsevier.com/locate/actamat

Full length article

# Electrochemical grinding-induced metallic assembly exploiting a facile conversion reaction route of metal oxides toward Li ions

Jiliang Zhang[a], Gi-Hyeok Lee[b,c], Vincent Wing-hei Lau[a], Feng Zou[a], Yingmin Wang[d], Xuelian Wu[e], Xun-Li Wang[e], Chi-Liang Chen[f], Chun-Jen Su[f], Yong-Mook Kang[a,g,*]

[a] Department of Materials Science and Engineering, Korea University, Seoul 02841, South Korea
[b] Department of Energy and Materials Engineering, Dongguk University-Seoul, Seoul 04620, South Korea
[c] Advanced Light Source, Lawrence Berkeley National Laboratory, Berkeley 94720, USA
[d] Key Laboratory of Materials Modification by Laser, Ion, and Electron Beams (Dalian University of Technology), Ministry of Education, & School of Materials Science and Engineering, Dalian University of Technology, Dalian 116024, Liaoning, PR China
[e] Department of Physics, City University of Hong Kong, 83 Tat Chee Ave., Kowloon, Hong Kong, PR China
[f] National Synchrotron Radiation Research Center, Hsinchu 30076, Taiwan R.O.C.
[g] KU-KIST Graduate School of Converging Science and Technology, Korea University, Seoul, 02841 Republic of Korea

ARTICLE INFO

*Article history:*
Received 9 October 2020
Revised 24 March 2021
Accepted 26 March 2021
Available online 2 April 2021

*Keywords:*
Li-ion battery
Microstructure
Metallic assembly
Short-range ordering
Conversion reaction

ABSTRACT

Conversion-type electrodes generally feature unstable cycling stability as an anode for Li ion batteries. In this work, however, we suggest that the weird capacity increase after initial decay during cycling is likely a common feature for the electrode materials undergoing high-rate conversion reaction. The cycling with $\alpha$-$Fe_2O_3$ anodes at the current density of 500 mA $g^{-1}$ or more could effectively trigger the typical capacity increase with cycle number after its initial degradation. Its morphological and structural evolutions during cycling are comprehensively characterized here by synchrotron X-ray scattering, X-ray absorption and photoelectron spectroscopies, and electron microscopy. The investigation demonstrates that enough fast conversion reaction tends to reduce the crystallite size of $\alpha$-$Fe_2O_3$ significantly as a result of the electrochemical grinding and the continuous cycling can generate the Fe-Fe-Fe medium-range ordering terminated by long Fe-O bonds, which exploits a facile conversion reaction route catalyzing the dissociation of $Li_2O$ toward lower redox potential and faster kinetics. In details, higher heterogeneity, larger stress/strain and thinner solid-electrolyte interphase layer accompanied by fast conversion reaction in $\alpha$-$Fe_2O_3$ can make its pristine crystallites smaller, finally extending the proportion of Fe-Fe-Fe ordering and thereby facilitating the conversion reaction for higher capacity during the following charge/discharge. Most importantly, the new structure enables excellent performance for the full cell, in contrast to the catastrophic failure of the pristine oxides. The structural evolution addressed in the study updates the understanding of conversion reactions and sheds light on novel types of conversion-type electrodes towards the full-cell application of conversion-reaction electrodes.

© 2021 Acta Materialia Inc. Published by Elsevier Ltd. All rights reserved.

## 1. Introduction

The commercial lithium-ion batteries (LIBs) have a difficulty to meet the continuously rising demand for higher power or energy densities and significantly extended cycling stability from portable electric devices and newly emerging large scale applications (e.g. electric vehicles and grid storage) [1]. One major obstacle falls in the graphite anodes, which suffer from low capacity (372 mAh $g^{-1}$) and energy density. Thus, enormous efforts have been made to develop novel anode materials with high capacity, most of which are based on conversion reactions and alloying reactions [2–4]. The elements or compounds governed by alloying reaction are limited [2], while the metal oxides-based candidates based on conversion reaction are numerous because of their diverse structures and constituents [5–7].

Despite the high theoretical capacity and coulombic efficiency of metal oxides, their poor electrical conductivity is against rapid electrochemical lithiation/delithiation, and the huge volume change typically accompanied by their conversion reactions leads to pulverization and loss of electrical contact during cycling, which is followed by a poor cycling stability [3,6,7]. In a typical conversion reaction, the parent particle is reduced into a composite of $Li_2O$ and metallic crystallites of 1-4 nm in size during lithiation and, upon delithiation, these metallic crystallites are oxidized into oxide crystallites of 1-4 nm, resulting from electrochemical

* Corresponding author.
*E-mail address:* dake1234@korea.ac.kr (Y.-M. Kang).

https://doi.org/10.1016/j.actamat.2021.116863
1359-6454/© 2021 Acta Materialia Inc. Published by Elsevier Ltd. All rights reserved.

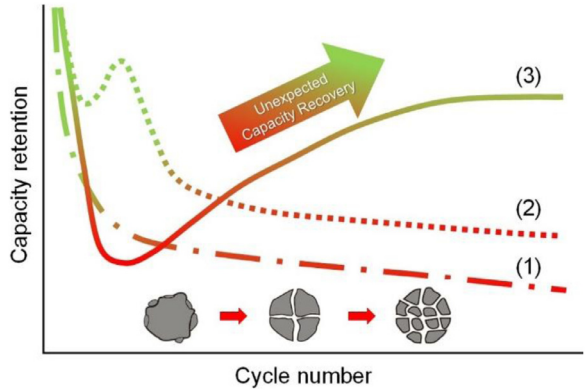


**Fig. 1.** Schematic illustration of the three types of cycling curves for conversion-type electrodes in the half-cell tests. (1) and (2) are mostly observed due to pulveriztion as illustrated below the curves, for example in $Fe_3O_4$ [16,21] and $CuCo_2O_4$ [9] respectively, while (3) is also seen in some cases generally without any explanation, for example in $Mn_3O_4$ [22].

grinding, even if the final shape of pristine particle is roughly maintained [8]. Therefore, it is very common to observe the sudden drop of capacity upon initial cycling (Fig. 1) with or without an activation process which shows a gradual capacity increment just after this initial drop [9]. Thus, much effort has been dedicated to overcoming these drawbacks, mainly including nanostructuring [10,11], porous or hollow structures [12,13], encapsulated or gyroidal structures [14,15], composite formation and doping various metallic elements [7,16,17]. It is generally accepted that nanostructured metal oxides effectively alleviate the large volume change resulting from the conversion reactions somewhat because the domain size of metallic parts segregated by lithiation is enough confined to catalyse the dissociation of $Li_2O$ during the following delithiation [18]. However, the control over the nanostructures is very complicated, and doping into nanomaterials may lead to the significant inhomogeneity, because doping elements are mainly distributed around the surface in most of cases [19,20]. The same problems of process complexity and inhomogeneity also exist in the fabrication of composites, which has the additional issue that many conducting agents (e.g. graphene and nanotubes) for composites are more expensive than the metal oxides themselves. Thus, the conversion electrode materials prepared by these strategies may not possess the advantage from the perspective of commercialization.

Among a lot of previous works on the conversion reaction between metal oxides and alkali ions, it has been typically noticed that the capacity of metal oxides electrodes unexpectedly rises up to some values even larger than their initial capacities after a dramatic capacity fading during first dozens of cycles, following a behaviour similar to the curve (3) in Fig. 1 [22–27]. Such a gradual capacity rise after its initial drop must be different from the typical activation behaviour of conversion reaction immediately followed by a drastic capacity fading as in curve (2) of Fig. 1. This phenomenon has been also observed in other kinds of conversion-reaction materials such as phosphides, sulfides, and their composites for both LIBs and sodium-ion batteries [28–30]. Understanding and exploiting these phenomena look essential to innovate the conversion reaction toward high energy-density batteries and design durable conversion reaction-based electrodes. However, up to now, it is still unclear what the specific mechanism for such capacity increase and drop is. Actually, there have been few comprehensive studies concerning this issue, even if it is critical to make the conversion reaction useful for high capacity anode materials.

In this work, $\alpha$-$Fe_2O_3$ (referred to as $Fe_2O_3$ thereafter), one of the most popular transition metal oxides, is employed to explore the specific mechanism for the rise and fall of capacity with the conversion reaction during cycling. Herein, comprehensive characterizations and analyses demonstrate how the structural evolution into the Fe-Fe-Fe medium-range ordering is induced by electrochemical grinding, which is primarily correlated to the capacity increase upon cycling. We come to be sure that this phenomenon is likely a common feature for conversion-type anodes, and offers the possibility to design highly durable and kinetic anode materials based on conversion reaction.

## 2. Experimental

### 2.1. Synthesis

An aqueous solution (55 ml) of 2.703 g $FeCl_3.6H_2O$ (10 mM, Sigma Aldrich, >97%) was first stirred for 30 minutes, and then precipitated with 28% aqueous ammonia (15 ml). After precipitation, the suspension was stirred for a further 30 minutes, and then transferred into a 100 ml Teflon-lined autoclave for hydrothermal reactions performed at 200 °C for 5 hours. The product was isolated by filtration, washed several times with distilled water and then with ethanol, and finally dried at 60 °C for 12 hours in an oven, followed by heat treatment at 300 °C for 3 hours.

### 2.2. Characterization

Important samples were selected for synchrotron XRD measurement in capillary mode. Powdered samples were loaded into 0.3 mm capillaries for uniform absorption and faster rotation during data collection. The high-resolution data were collected at TPS 09A (Taiwan Photon Source) of the National Synchrotron Radiation Research Center. The 15 keV X-ray source (wavelength 0.826569Å) is delivered from an in-vacuum undulator (IU22) and the powder diffraction patterns were recorded by a position-sensitive detector, MYTHEN 24K, covering a $2\theta$ range of 120°. Due to the small gaps between detector modules, two data sets were collected 2° apart with a 60 second exposure time and the data were merged and gridded to give a continuous data set. Structural analyses on XRD data were performed using Topas-Academic (Version 6).

XAS spectra were collected on the beamline 17C1 at Taiwan Light Source, and the beamline 10C in Pohang Accelerator Laboratory. Fe *K*-edge XAS data were acquired in transmission mode and an iron foil was used as an internal energy calibration where the first reflection point was defined to be 7112.0 eV. Data reduction and analysis were performed using the programs in Demeter software package [31]. The SAXS measurements were performed on the beamline 23A at Taiwan Light Source, with high-flux collimated X-ray of 15 keV and a beam size of ca. 500 $\mu$m.

The morphology and microstructure were inspected using a high-resolution transmission electron microscope (JEOL, JEM-3100 with an acceleration of 300 kV). Element-specific electronic properties were determined by X-ray photoelectron spectroscopy using an ULVAC-PHI 5802 spectrometer equipped with a monochromatized Al K$\alpha$ radiation ($h\nu$=1486.6 eV) in vacuum of about $10^{-9}$ mbar. The thickness of ion sputtering was referenced to silicon dioxide on silicon wafers. Adventitious carbon was used for calibration by setting the main line of C 1*s* spectrum to 284.8 eV. The resolution is 0.1 eV for high resolution spectra.

### 2.3. Electrochemical measurements

Electrochemical experiments were carried out by using CR-2032 coin cells, which were assembled in a glovebox under Ar atmosphere, using metallic lithium foil as the counter electrode. The working electrode in this work was prepared from a slurry consisting of the active material (70 wt%), carbon SuperP (20 wt%)

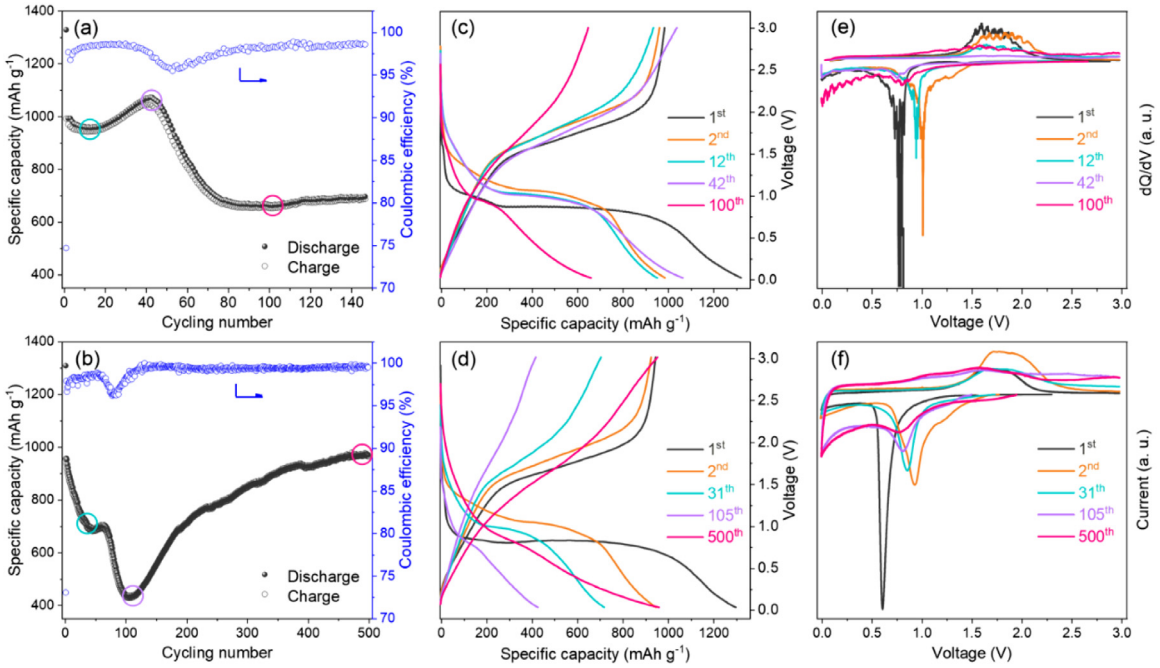


**Fig. 2.** Electrochemical properties of $Fe_2O_3$. Cycling performance and galvanostatic discharge/charge plots are collected at different current densities: (a) and (c) at 100 mA $g^{-1}$, and (b) and (d) at 500 mA $g^{-1}$. (e) shows the derivative (dQ/dV) of galvanostatic plots in (d), and (f) presents the cyclic voltammograms (CV) of electrodes after different cycles at 500 mA $g^{-1}$.

and PVDF (10 wt%), cast on copper foil. Celgard 2400 microporous polypropylene membrane was used as the separator, while a solution of 1M $LiPF_6$ in ethylene carbonate (EC) and diethyl carbonate (DEC) (1:1 by volume) was employed as the electrolyte. The galvanostatic charge-discharge cycling test and cyclic voltammetry were conducted using a WBCS battery test system (WonATech) at ambient temperature.

## 3. Results

The $Fe_2O_3$ samples obtained by a hydrothermal reaction followed by a heat treatment at 300 °C is initially phase-pure, as confirmed by the Rietveld refinement on the synchrotron powder X-ray diffraction data (PXRD, see **Figure S1** in Supplementary Material). These as-obtained samples were then used as anodes in half-cell LIBs to explore the reason for the cycling-enhanced capacity variations.

### 3.1. Electrochemical behaviours

The cycling performance of these half-cell LIBs was evaluated with different current densities from 100 mA $g^{-1}$ to 1000 mA $g^{-1}$. At 100 mA $g^{-1}$ (Fig. 2a), the reversible discharge capacity was 1000(6) mAh $g^{-1}$ in 1$^{st}$ cycle and showed a slow decrease during about initial 10 cycles followed by a gradual increment up to a maximum of ca. 1100 mAh $g^{-1}$ after 40 cycles. Then the capacity fades quickly to a stable value of 656(6) mAh $g^{-1}$ after 80 cycles. This phenomenon of increasing/decreasing capacity with cycling is the case described by the curve (2) in Fig. 1. In the literature, the valley-like capacity change from 1$^{st}$ to the 40$^{th}$ cycle is attributed without any solid evidence to an activation process associated with size refinement by conversion reactions [32]. Further increase in current density to 300 mA $g^{-1}$ led to a significant capacity fading in 80 cycles, and then the very sluggish capacity increase was observed upon further cycling (**Figure S2**).

When the current density is increased to 500 mA $g^{-1}$ (Fig. 2b), the specific capacity dramatically decreases by around the 105$^{th}$ cycle to a minimum value. On the way, $Fe_2O_3$ goes through a small valley in the ca. 31$^{th}$ cycle, and then an activation process similar to that at a current of 100 mA $g^{-1}$. Further cycling led to gradual capacity increase, being stabilized at 963(7) mAh $g^{-1}$ after 477(2) cycles. Cycling at 1000 mA/g makes the gradual capacity increase faster and it reaches a stable capacity earlier at around 220 cycles (**Figure S2**). It should be also noted that the final stable capacity achieved at 1000 mA $g^{-1}$ is ca. 750 mAh $g^{-1}$, much less than 963 mAh $g^{-1}$ at 500 mA $g^{-1}$. Compared with the cycling before the minimum capacity, the further looks more stable with the increased capacity and much higher coulombic efficiency of ca. 99%. The cycling-enhanced capacity increment at high current densities has been reported mainly in porous oxides and oxides composites with conductive agents [27,33,34]. Without any solid evidence, three simple explanations on the phenomenon have been proposed in the literature as follows: 1) phase transitions (e.g. $\alpha$-$Fe_2O_3$ to $\gamma$-$Fe_2O_3$ and finally $\beta$-$Fe_2O_3$) [33]; 2) interfacial storage [35]; and 3) electrolyte degradation [36]. The reported phase transition in $\alpha$-$Fe_2O_3$ anodes is based on ambiguous XRD results [33]. Furthermore, $\gamma$-$Fe_2O_3$ anodes also exhibit similar cycling-enhanced capacity behaviour and the $\gamma$-$Fe_2O_3$ phase is still observed after 1000 cycles, which indicates that the phase transition to its polymorphs has nothing to do with the capacity changes upon cycling [37]. The reduced particle size with cycling makes more surface exposed enhancing its capacity, based on the second mechanism, but it can give rise to significant irreversible capacity rather than reversible capacity. Electrolyte degradation can contribute to extra apparent capacity, but simultaneously lead to a low coulombic efficiency not observed here. Hence, none of these three mechanisms looks satisfactory.

The discharge-charge curve for the stable capacity (i.e. 100$^{th}$ cycle) at 100 mA $g^{-1}$ is characterized by a significantly reduced potential plateau, while the capacity in low potential region increases a lot (**Figures 2c, 2d and S3**). By contrast, at 500 mA $g^{-1}$, the length of plateau is continuously reduced finally reaching the minimum in 105$^{th}$ cycle, while no evident increase of capacity is observed in low potential region (**Figure S4**). During further cycles,

the capacity from this region monotonically increases up to a stable value after 477 cycles, reaching around the theoretical value. Such a change is more clear in the differential plot of capacity (dQ/dV) as shown in Fig. 2e. The peak value of dQ/dV is continuously shifted towards low potentials upon cycling, which may be ascribed to the gradually reduced crystallite sizes [32,38,39]. A major contribution to the increased capacity may be attributed to the enhanced non-faradaic reaction resulting from the corresponding pulverization and the subsequent reduction of crystallite size.

The cyclic voltammetry (CV) curves at 500 mA $g^{-1}$ were also collected at a scan rate of 0.1 mV $s^{-1}$ (Fig. 2f). The CV curve of pristine $Fe_2O_3$ is similar to that reported in many literature [7,33,40]: a strong cathodic peak at ca. 0.63 V and a broad anodic peak located at 1.7 V. After 1st cycle, the main cathodic peak is shifted to 0.98 V, due to the activation of pristine materials, while the anodic peak shows no evident shift. In further cycles, the cathodic peak is slightly shifted toward low potentials, in accordance with the literature [33,40]. However, in the CV here, a new anodic peak at 1.1 V appears after 105 cycles, suggesting the redox of $Fe^0$ into the Fe ions, rather than the formation of any $Fe_2O_3$ polymorph. The redox reaction at such low oxidation potential may also be related to the formation of new crystalline ordering, accounting for the capacity increase.

### 3.2. Morphological and microstructural changes

Ex situ PXRD data show only Bragg reflections of $Li_2CO_3$ from the SEI layer and the tiny amount of unreacted $Fe_2O_3$ after 1st cycle (**Figures S5** and **S6a**, see details in Supplementary Material), suggesting the evolution of ultrasmall crystallite [41]. By comparing the patterns of empty capillaries, the two diffraction humps from cycled $Fe_2O_3$ can be determined from the deconvolution (**Figure S6b** and **Table S1**). According to the deconvolution after 1st cycle, more than 95% of $Fe_2O_3$ is reacted and the crystallite size was estimated as ca. 4 nm, while the peak shift of reacted $Fe_2O_3$ suggests larger strain/stress induced during charge/discharge. During further cycling (e.g. after 105 cycles), these diffraction humps are significantly diminished and cannot be distinguished, suggesting further reduction of crystallite size or/and possible phase transitions to other structures. However, absence of extra reflection in the PXRD patterns of these cycled samples indicates that the crystallites in new phases should be very tiny. The Rietveld refinements on PXRD data after 105 cycles confirm that Bragg reflections are mainly from $Li_2CO_3$ and the unreacted $Fe_2O_3$ is ca. 1 % of $Li_2CO_3$ in weight, while all Bragg reflections can be fitted using only $Li_2CO_3$ after 500 cycles.

Because the presence of ultrasmall crystallites (< 4 nm) was not detected in PXRD data, exsitu TEM was then employed to examine the details of morphological and structural changes in these samples. For the pristine sample, the bright-field TEM image (Fig. 3a) shows that $Fe_2O_3$ particles are of diamond-like shape with a mean size of 150 nm, and the corresponding SAED pattern reveals the single crystal nature of the individual particle with (006) planes (**Figure S7a**). After 1st cycle, the particle size does not change much, while the particle shape is evidently elongated along the diagonal direction (Fig. 3b). The fine dots inside the particles are the refined $Fe_2O_3$ crystallites of 3-4 nm (**Figure S7b**), whose size is similar to those observed in the literature [8]. High resolution TEM images also indicate that a high density of structural faults exists inside the single particle. After 31 cycles, the crystallites are further refined by the electrochemical grinding phenomenon, as characterized by the discontinuous ring feature of the diffraction pattern (Fig. 3c). In the electrodes subjected to 105 cycles, the particles are broken into pieces and crystallites of ca. 2 nm are formed significantly, generating irregular particle shapes and even finer particle sizes (**Figures 3d** and S7c). The high resolution TEM images show that the lattice fringes in the single crystallite are actually strongly distorted. After 500 cycles, most of the $Fe_2O_3$ particles have irregular shapes with a size of 20-50 nm (Fig. 3e and S7d), which produce a rather continuous polycrystalline ring pattern. The sharp spots in the SAED pattern are likely due to $Li_2CO_3$, while a few weak polycrystalline rings other than those from $Fe_2O_3$ are also observed (see the arrow in Figure S7d), suggesting the formation of unknown phases with similar or even smaller crystallite sizes. Compared with a thick SEI layer of ca. 50 nm after 100 cycles at a low current density of 100 mA $g^{-1}$ (Fig. 3f), the SEI layer of the electrodes cycled at 500 mA $g^{-1}$ is much thinner and even extended cycling does not significantly increase the thickness. The thinner SEI layers on the surface are also supported by ex situ X-ray photoelectron spectroscopy (XPS) data (**Figures S8-S12**), while $O^{2-}$-vacancy-like signals become more evident in XPS data of the bulk structure after 105 cycles (**Figure S13)**.

In addition to TEM images, ex situ SAXS data were also collected to verify that the above results. As shown in Fig. 3g, a peak is observed in the Q range of 0.13-0.45 $nm^{-1}$ (corresponding to 15-50 nm in size) after 500 cycles, in agreement with the particle size in the TEM images (Fig. 3e). Close examinations on these data show that the peak already appears after 105 cycles, but has a very weak intensity. Nevertheless, no obvious step or peak is observed in the high Q zone (1-3 $nm^{-1}$ corresponding to 2-6 nm in size, **Figure S14**) of these SAXS plots, although the signals for crystallizes and components in SEI layers are expected in the zone. The amorphous carbon and the polyvinylidene fluoride (PVDF) binder in electrodes possibly make signals in the region too broad.

### 3.3. Structural evolution

To more examine the structural information, ex-situ Fe *K*-edge X-ray absorption spectra (XAS) were also collected. According to X-ray absorption near-edge spectra (XANES) shown in Fig. 4a, the pre-edge (i.e. the peak at ca. 7114 eV) shifts towards lower energy with cycles, corresponding to lower oxidation states of Fe ions. The XANES data for the cycled electrodes were well fit with a linear combination of Fe metal ($Fe^0$), FeO, $Fe_3O_4$ and $Fe_2O_3$ gave satisfying results for these cycled electrodes except 1st cycle (Fig. 4b and **Table S2**). The poor fit for the electrode after 1st cycle implies that the local structure of Fe here is different from that in these known Fe species. After 31 cycles, significant amounts of $Fe_3O_4$-like Fe species appear and are converted into $Fe^0$-like species gradually during subsequent cycles.

In the Fourier transformations of the extended X-ray absorption fine structure (EXAFS) spectra of pristine $Fe_2O_3$ (Fig. 4c), there are two groups of strong signals, one at 0.8-2.1 Å corresponding to the nearest Fe-O bond and another at 2.01-3.8 Å for two kinds of Fe-Fe distances [42]. After 1st cycle, the peak for Fe-Fe distances gets very weaker, likely due to the disordering from the large strain induced by the fast conversion reaction [43]. Such disordering also accounts for the poor linear combination fit (LCF) on the XANES data. Further cycling leads to an obvious signal for the nearest Fe-Fe distance after 31 cycles, but the signal is much weaker than the one in the pristine $Fe_2O_3$ and the signals associated with longer distances of 3-4 Å are still absent. Therefore, this Fe-Fe signal should not come from $Fe_2O_3$ but the $Fe_3O_4$-like species, suggesting the structural reordering of Fe-O-Fe.

Further cycles (i.e. 105 cycles and beyond), surprisingly, introduce several extra peaks at larger radial distances together with the continuous shifts of two main signals for Fe-O and Fe-Fe bonds. Remarkably, the Fe-Fe signals of radial distance larger than 2 Å in these extensively cycled electrodes are much shorter than those in all oxides but very similar to those in Fe metals (**Figures 4c and S15**), which is consistent with the $Fe^0$-like species observed from the LCF on the XANES data (**Table S2**), while an evident signal ap-

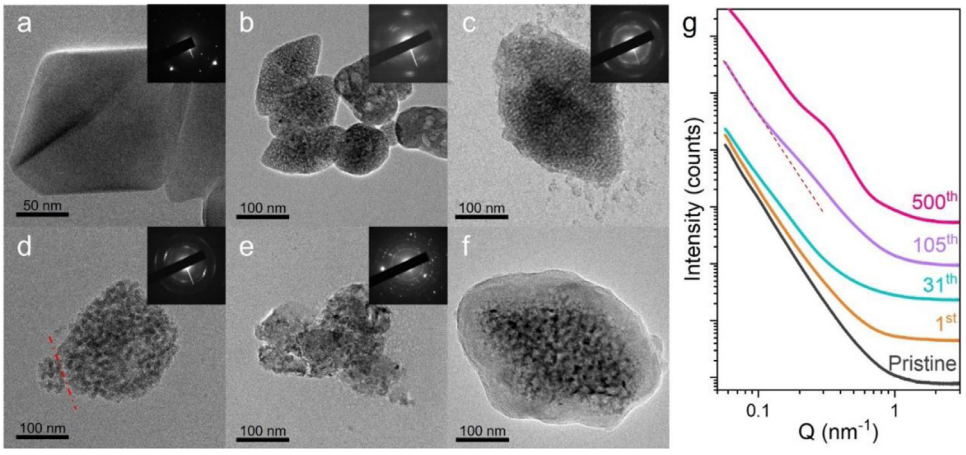


**Fig. 3.** TEM images and the corresponding SAED patterns of $Fe_2O_3$ electrodes after different cycles at 500 mA $g^{-1}$: a) pristine; b) 1 cycle; c) 31 cycles; d) 105 cycles and e) 500 cycles. The TEM image of the electrode after 100 cycles at a lower current density of 100 mA $g^{-1}$ is also given for comparison (f). The ex situ SAXS patterns after different cycles are plotted in (g). The bright diffuse ring in the inset of (c) is from the carbon additive in electrodes. The dashed line in (d) marks the interface between a broken piece and the parent particle.

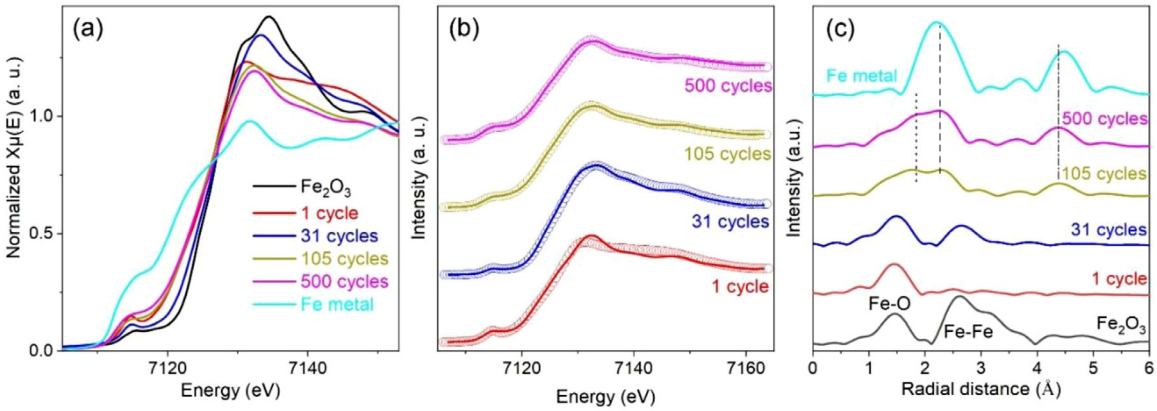


**Fig. 4.** XAS spectra of $Fe_2O_3$ electrodes after different cycles. The XANES data and the corresponding linear combination fit (LCF) are shown in (a) and (b) respectively, while the Fourier transform of EXAFS data is given in (c) without phase-shift correction. The circles are for experimental data while the solid lines show the fits in (b). The dash and dot-dash lines in (c) emphasize the peak shift compared with those in Fe metal, while the dotted line emphasizes a new signal for much longer Fe-O distances compared to those in $Fe_2O_3$.

peared at a large redial distance of ~4.4 Å is not common in oxides but similar to that in Fe metals. These results clearly suggest the formation of Fe-Fe-Fe with a medium-range order (MRO), which is similar to that in Fe metals in these cycled electrodes. Compared with Fe metals, the nearest Fe-Fe distance in these electrodes is lightly longer while the Fe-Fe distance at larger radial distances (e.g. ~4.4 Å) is a little shorter. Such a distortion, together with the simultaneous variation of Fe-O distance, indicates that the abnormal Fe-Fe-Fe ordering in the electrodes should correspond to a new phase terminated with oxygen enabling a longer Fe-O distance. In other words, the new phase can be classified into a kind of iron oxide, comprising the Fe-Fe-Fe MRO terminated by oxygen atoms to avoid the oxidation of $Fe^0$ during the subsequent charge/discharge. The low coordination number of these oxygen centers as suggested by the increased $O^{2-}$-vacancy-like XPS signals accounts for the large O to Fe ratio, which helps to retain the high capacity during extended cycling.

To figure out the structural information of phases evolved after different cycles, some efforts were dedicated to fit these EXAFS data. The structural model based $Fe_2O_3$ yields reliable fits on the electrodes before and after 1st cycle (**Figure S16**). The fitted Fe-O distance in the pristine electrodes is 1.965 Å, in good accordance with the results of Rietveld refinements, while the fitted Fe-O distance after 1st cycle is 1.9068 Å and the reduced distance is consistent with the peak shift in the synchrotron XRD data (**Figure S6b**). However, it was difficult to get reliable fits on the electrode after 31 cycles. Therein, multiple phases already exist after 31 cycles and their structural information is not available from XRD data because of its ultrasmall crystallite sizes (**Figures S6c and S6d**), resultantly making any reliable fitting unfeasible.

With the formation of the Fe-Fe-Fe ordering (e.g. after 105 cycles), a new signal ascribed to longer Fe-O distance is observed simultaneously in all the cycled electrodes (Fig. 4c). Because the radial distance is much longer than typical Fe-O bonds in most of iron oxides (**Figure S15**), the new Fe-O signal should result from longer Fe-O bonds of the new phase rather than the simple elongation of Fe-O bonds in $Fe_2O_3$ or $Fe_3O_4$ when the huge structural change driven by conversion reaction is considered. Such long Fe-O bonds and low coordination number are generally the feature of oxygen atoms at the surface [44]. However, the EXAFS data suggest that these oxygen atoms are engaged in the bulk structure, while the enhanced oxygen vacancy from XPS demonstrates the low coordination number of these oxygen atoms (**Figure S13**). Therefore these terminating oxygen atoms should not locate on the surface but have a low coordination number, in agreement with the inferred new structure in Fig. 4. The Fe-Fe distance closer to that in Fe metal and further elongated Fe-O distance after 500 cycles demonstrates that the extended cycling can reduce the distortion

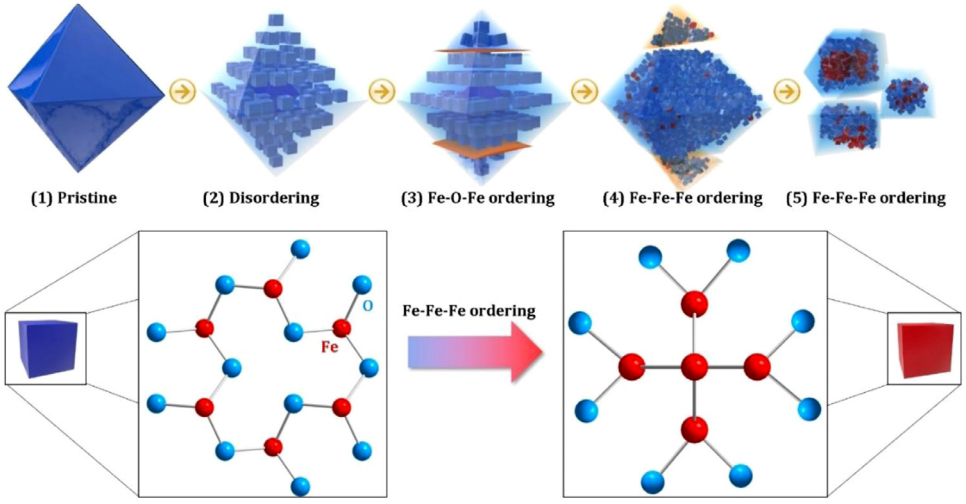


**Fig. 5.** Schematic illustration on the morphological and structural evolution during cycles. Five stages of morphological evolution on the top roughly correspond to the pristine particle, and particles after 1, 31, 105 and 500 cycles respectively, while the structural variation is explained in words below the schematic morphology. Yellow zones show high-angle grain boundaries or high stresses. The red particles represent the new structure, while the bottom illustrates the change from $Fe_2O_3$ to the new structure in 2 dimensions.

of the new structure with an increased concentration (**Table S2**), accounting for the capacity rise.

The Fe-Fe-Fe MRO in the new phase enables Fe-Fe direct magnetic exchange interaction and thus strong magnetization is expected compared with the very weak long-range Fe-O-Fe superexchange interaction in $Fe_2O_3$. The pristine $Fe_2O_3$ is ferromagnetic but the magnetization is too weak without any visible response to a magnet. This magnetic property appears to be maintained after 31 cycles also show no response, but the electrodes after 105 cycles could be attracted by a magnet, affirming the presence of the Fe-Fe-Fe MRO.

## 4. Discussion

According to the above experimental results, the morphological and structural evolution during the high-rate electrochemical cycling can be illustrated in Fig. 5 schematically. The high current density leads to not only incomplete reaction as suggested by ex situ XRD data but also large lattice strains due to the volume change and electrochemical grinding after 1$^{st}$ cycle (from stage 1 to 2 in Fig. 5). The large strain accounts for the strong disordering of Fe, characterized by the absence of Fe-Fe signals in the EXAFS data and in contrast to the evident signal from $Fe_2O_3$ in the cycled sample at a lower current density (e.g. 20mA $g^{-1}$) [42].

Further cycling will continuously refine crystallite sizes and create more grain boundaries for larger strains (stage 3), leading to the quick capacity decay. The larger strains enable high-angle boundaries (see yellow zones in Fig. 5), and may drive the highly disordered Fe reordering (i.e. the $Fe_3O_4$-like ordering after 31 cycles). When the crystallite size is reduced to a critical value, which is comparable to the size of the unit cell (ca. 1-2 nm see **Figure S5**), the reduced product of this crystallite contains only dozens of Fe atoms. Thus during the following cycles, these surface Fe atoms can be easily oxidized at lower redox potentials [45], while the inner Fe-Fe interactions are kept to form a new structure featured by the Fe-Fe-Fe MRO, which is similar to that in body-centered cubic Fe and terminated by oxygen.

The high-angle grain boundaries and the lattice mismatch between the crystallites of reordered structure and distorted $Fe_2O_3$ generate cracks during cycling finally pulverizing it (stage 4). During subsequent cycles, more particles are broken into smaller pieces of 20-50 nm (stage 5). The reduced particle size allows the complete reaction with Li even at the high rate (**Figure S5**), continuously increasing the new phase. Similar cycling-enhanced capacity behaviour is also observed in $Fe_2O_3$ nanoparticles of 40-60 nm in size despite the low triggering current density (e.g. 200 mA $g^{-1}$) [46]. Therefore, rather than the reduced particle size, the evolution of new structure could be plausible reason for the capacity rise as demonstrated by the increased concentration of the new phase from 105$^{th}$ cycle to 500$^{th}$ cycle (**Table S2**).

According to XAS analysis, the new phase associated with Fe-Fe-Fe MRO was already formed before reaching minimum capacity, while the fraction of Fe species corresponding to the new phase is only 38(2)% after the steady capacity (i.e. 500cyles). Thus a critical concentration of the new phase can explain the capacity rise, because it functions as both capacity sources and catalyst for conversion reactions. In spite of the Fe-Fe-Fe MRO, the terminating oxygen results in a high oxygen concentration in the new phase (i.e. Fe:O=5:8 for the schematic structure in Fig. 5). The long Fe-O bond in the new structure looks beneficial for bond breaking and reforming, whereas the sub-nanometer Fe precipitated during discharge enables much higher catalytic activity for the conversion reaction compared to bulk Fe and its surface sites [47,48]. All these features synergistically realize the excellent high-rate electrochemical performance observed after 500 cycles.

Based on the above discussion, the disordered structure induced by large strain looks like a key to evolve into the new structure, while the thin SEI layer helps the particle size of crystallites to be reduced toward the capacity rise. In contrast, the well-ordered $Fe_2O_3$ is still maintained after cycles at relatively low current density (e.g. 20 mA $g^{-1}$), as proven by the XRD reflections and EXAFS signal for Fe-Fe interatomic distance [42]. Thus the driving force for the structural reordering is lacking in this case and the thick SEI layer prevents the particle into being reduced to smaller pieces.

The cycling-induced capacity increase is observed in many oxide anodes but only within half-cell tests. In the full cell, the amount of Li ions is limited by those in cathode and therefore it is important to explore the application of such a phenomenon in the full cell. Unfortunately, the fresh $Fe_2O_3$ anode shows only catastrophic capacity decay (**Figures 6** and **S17**). Meanwhile, the anodes after 500 cycles in the half-cell test (see Fig. 2b) exhibit a stable capacity retention (ca. 600 mAh $g^{-1}$ after 70 cycles) as shown in Fig. 6 and the cycled electrode look also stable in air atmosphere (**Figure S18**).

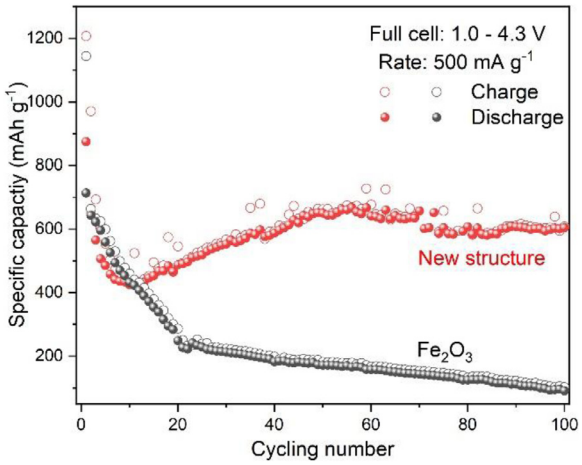


**Fig. 6.** Cycling performance of full cells using $LiCoO_2$ cathodes. The new structure refers to the anode after 500 cycles in the half cell (see Fig. 2b).

To verify the applicability of this strategy to the full cells of other oxide anodes, the commercial NiO was also chosen for further investigation. As expected, the cycling-induced capacity increase was observed at a current density of 500 mA $g^{-1}$. This cycled NiO anode also exhibits excellent cycling stability in the full cell, other than the catastrophic failure of fresh NiO anodes (**Figure S19**). This study suggests that the fast electrochemical grinding can be an effective way to obtain new structure composed of metallic medium-range ordering for a facile conversion reaction, which is capable of innovatively increasing the energy density of LIBs.

## 5. Conclusions

A systemic investigation here showed that the $Fe_2O_3$ electrodes cycled at a large current density of 500 mA $g^{-1}$ undergo the cycling-induced capacity increase, which is triggered by fast conversion reaction. It could effectively grind the size of crystallites into a critical size comparable to the unit cell of $Fe_2O_3$, resultantly generating large lattice strain to make the structural reordering happen and stabilizes Fe-Fe-Fe MROs terminated by oxygen atoms via longer Fe-O bonds. This new structure has a low redox potential as well as several remarkable electrochemical advantages presented by the cycling-induced capacity rise. Most importantly, the new structure also exhibits excellent high-rate performance in full cells, other than the catastrophic failure of pristine $Fe_2O_3$. Such structural evolution induced by electrochemical grinding, which leads to the capacity increase with cycling seems to be a common feature for the conversion reaction of metal oxides. This result not only allows a better understanding of capacity rising during cycling typically observed in conversion-type electrodes but also supplies an innovative way to develop novel class of electrode materials. The new structure with Fe-Fe-Fe MROs may also be promising for catalytic and magnetic applications. However, this new structure needs to be investigated in details to figure out its clear crystal structure and various properties. For example, a systematic investigation on the high-rate conversion reaction of transition metal oxides with different morphologies or microstructures may be very helpful. Because the ball milling can also introduce large strains and break the particle into smaller pieces, the intensive ball milling may be an alternative way to produce this kind of structures.

## Declaration of Competing Interest

None.

## Acknowledgments

This work was supported by the National Research Foundation funded by the Ministry of Science, ICT, and Future Planning, Republic of Korea, under “First Research in Lifetime” grant (NRF-2018R1C1B5047313), “Middle Career Program” grant (NRF-2017R1A2B3004383), “Science Research Centre” grant (NRF-2017R1A5A1015365), and “Future Materials Discovery” grant (NRF-2020M3D1A1110527). G.-H.L. acknowledge the financial support of the ALS fellowship program. X-ray absorption spectroscopy data were collected at TLS-17C1 beam line in National Synchrotron Radiation Research Center (NSRRC) in Taiwan and PLS-II 10C in Pohang Accelerator Laboratory. We acknowledge the support teams for assistance at TPS 09A and TLC 23A in NSRRC.

## Supplementary materials

Supplementary material associated with this article can be found, in the online version, at doi:10.1016/j.actamat.2021.116863.

## References

[1] J.B. Goodenough, Electrochemical energy storage in a sustainable modern society, Energy Environ. Sci. 7 (1) (2014) 14–18, doi:10.1039/C3EE42613K.
[2] C.-M. Park, J.-H. Kim, H. Kim, H.-J. Sohn, Li-alloy based anode materials for Li secondary batteries, Chem. Soc. Rev. 39 (8) (2010) 3115–3141, doi:10.1039/B919877F.
[3] S.-H. Yu, X. Feng, N. Zhang, J. Seok, H.D. Abruña, Understanding conversion-type electrodes for lithium rechargeable batteries, Acc. Chem. Res. 51 (2) (2018) 273–281 273-281, doi:10.1021/acs.accounts.7b00487.
[4] D. Puthusseri, M. Wahid, S. Ogale, Conversion-type anode materials for alkali-ion batteries: state of the art and possible research directions, Acs Omega 3 (4) (2018) 4591–4601, doi:10.1021/acsomega.8b00188.
[5] Y. Idota, T. Kubota, A. Matsufuji, Y. Maekawa, T. Miyasaka, Tin-based amorphous oxide: a high-capacity lithium-ion-storage material, Science 276 (5317) (1997) 1395–1397, doi:10.1126/science.276.5317.1395.
[6] K. Zhang, X. Han, Z. Hu, X. Zhang, Z. Tao, J. Chen, Nanostructured Mn-based oxides for electrochemical energy storage and conversion, Chem. Soc. Rev. 44 (3) (2015) 699–728, doi:10.1039/C4CS00218K.
[7] J. Zhang, V.W.-h. Lau, C.-Z. Liao, K.W. Wong, G.-H. Lee, F. Zou, C.-K. Chang, H.-S. Sheu, Y.-M. Kang, Controlling the valence state of Cu dopant in $\alpha$-Fe2O3 anodes: effects on crystal structure and the conversion reactions with alkali ions, Chem. Mater. 31 (4) (2019) 1268–1279, doi:10.1021/acs.chemmater.8b03977.
[8] P. Poizot, S. Laruelle, S. Grugeon, L. Dupont, J.M. Tarascon, From the vanadates to 3d-metal oxides negative electrodes, Ionics 6 (5) (2000) 321–330, doi:10.1007/BF02374148.
[9] M. Bhardwaj, A. Suryawanshi, R. Fernandes, S. Tonda, A. Banerjee, D. Kothari, S. Ogale, $CuCo_2O_4$ nanowall morphology as Li-ion battery anode: enhancing electrochemical performance through stoichiometry control, Mater. Res. Bull. 90 (2017) 303–310, doi:10.1016/j.materresbull.2016.12.014.
[10] Z. Wang, L. Zhou, X.W. Lou, Metal oxide hollow nanostructures for lithium-ion batteries, Adv. Mater. 24 (14) (2012) 1903–1911, doi:10.1002/adma.201200469.
[11] K.M. Nam, J.H. Shim, D.-W. Han, H.S. Kwon, Y.-M. Kang, Y. Li, H. Song, W.S. Seo, J.T. Park, Syntheses and characterization of Wurtzite CoO, rocksalt CoO, and spinel $Co_3O_4$ nanocrystals: their interconversion and tuning of phase and morphology, Chem. Mater. 22 (15) (2010) 4446–4454, doi:10.1021/cm101138h.
[12] S.M. Hwang, Y.-G. Lim, J.-G. Kim, Y.-U. Heo, J.H. Lim, Y. Yamauchi, M.-S. Park, Y.-J. Kim, S.X. Dou, J.H. Kim, A case study on fibrous porous SnO2 anode for robust, high-capacity lithium-ion batteries, Nano Energy 10 (2014) 53–62, doi:10.1016/j.nanoen.2014.08.020.
[13] S.M. Hwang, S.Y. Kim, J.-G. Kim, K.J. Kim, J.-W. Lee, M.-S. Park, Y.-J. Kim, M. Shahabuddin, Y. Yamauchi, J.H. Kim, Electrospun manganese–cobalt oxide hollow nanofibres synthesized via combustion reactions and their lithium storage performance, Nanoscale 7 (18) (2015) 8351–8355, doi:10.1039/C5NR01145K.
[14] H. Xue, J. Zhao, J. Tang, H. Gong, P. He, H. Zhou, Y. Yamauchi, J. He, High-loading nano-SnO2 encapsulated in situ in three-dimensional rigid porous carbon for superior lithium-ion batteries, Chem. – A Eur. J. 22 (14) (2016) 4915–4923 https://doi.org /10.1002/chem.201504420.
[15] J. Lee, J. Moon, S.A. Han, J. Kim, V. Malgras, Y.-U. Heo, H. Kim, S.-M. Lee, H.K. Liu, S.X. Dou, Y. Yamauchi, M.-S. Park, J.H. Kim, Everlasting living and breathing Gyroid 3D network in Si@SiOx/C nanoarchitecture for lithium ion battery, ACS Nano 13 (8) (2019) 9607–9619, doi:10.1021/acsnano.9b04725.
[16] M.R. Jo, J. Jung, G.-H. Lee, Y. Kim, K. Song, J. Yang, J.S. Chae, K.C. Roh, Y.-I. Kim, W.-S. Yoon, Y.-M. Kang, $Fe_3O_4$ nanoparticles encapsulated in one-dimensional $Li_4Ti_5O_{12}$ nanomatrix: an extremely reversible anode for long life and high capacity Li-ion batteries, Nano Energy 19 (2016) 246–256, doi:10.1016/j.nanoen.2015.10.032.
[17] K.M. Nam, Y.C. Choi, S.C. Jung, Y.-I. Kim, M.R. Jo, S.H. Park, Y.-M. Kang, Y.-K. Han, J.T. Park, [100] Directed Cu-doped h-CoO nanorods: elucidation of the

growth mechanism and application to lithium-ion batteries, Nanoscale 4 (2) (2012) 473–477, doi:10.1039/C1NR11128K.
[18] C. Wu, P. Yin, X. Zhu, C. OuYang, Y. Xie, Synthesis of hematite ($\alpha$-$Fe_2O_3$) nanorods: diameter-size and shape effects on their applications in magnetism, lithium ion battery, and gas sensors, J. Phys. Chem. B 110 (36) (2006) 17806–17812, doi:10.1021/jp0633906.
[19] F. Ulu Okudur, J. D'Haen, T. Vranken, D. De Sloovere, M. Verheijen, O.M. Karakulina, A.M. Abakumov, J. Hadermann, M.K. Van Bael, A. Hardy, Ti surface doping of $LiNi_{0.5}Mn_{1.5}O_{4-\delta}$ positive electrodes for lithium ion batteries, RSC Adv. 8 (13) (2018) 7287–7300, doi:10.1039/C7RA12932G.
[20] S. Liu, Z. Liu, X. Shen, W. Li, Y. Gao, M.N. Banis, M. Li, K. Chen, L. Zhu, R. Yu, Z. Wang, X. Sun, G. Lu, Q. Kong, X. Bai, L. Chen, Surface doping to enhance structural integrity and performance of Li-rich layered oxide, Adv. Energy Mater. 8 (31) (2018) 1802105, doi:10.1002/aenm.201802105.
[21] K. Song, Y. Lee, M.R. Jo, K.M. Nam, Y.-M. Kang, Comprehensive design of carbon-encapsulated $Fe_3O_4$ nanocrystals and their lithium storage properties, Nanotechnology 23 (50) (2012) 505401, doi:10.1088/0957-4484/23/50/505401.
[22] J. Ye, D. Zhao, Q. Hao, C. Xu, Facile fabrication of hierarchical manganese-cobalt mixed oxide microspheres as high-performance anode material for lithium storage, Electrochim. Acta 222 (2016) 1402–1409, doi:10.1016/j.electacta.2016.11.117.
[23] Y. Teng, H. Zhao, Z. Zhang, Y. Li, H. Liu, Self-assembly of flower-like $MoO_3$-NiO microspheres with carbon coating as high-performance anode material for lithium-ion batteries, Mater. Lett. 246 (2019) 141–143, doi:10.1016/j.matlet.2019.03.076.
[24] Y. Zhao, X. Li, J. Liu, C. Wang, Y. Zhao, G. Yue, MOF-derived $ZnO/Ni_3ZnC_{0.7}$/C hybrids yolk–shell microspheres with excellent electrochemical performances for lithium ion batteries, ACS Appl. Mater. Interfaces 8 (10) (2016) 6472–6480, doi:10.1021/acsami.5b12562.
[25] L. Lefrançois Perreault, F. Colò, G. Meligrana, K. Kim, S. Fiorilli, F. Bella, J.R. Nair, C. Vitale-Brovarone, J. Florek, F. Kleitz, C. Gerbaldi, Spray-dried mesoporous mixed Cu-Ni Oxide@Graphene nanocomposite microspheres for high power and durable li-ion battery anodes, Adv. Energy Mater. 8 (35) (2018) 1802438, doi:10.1002/aenm.201802438.
[26] Y. Huang, Z. Xu, J. Mai, T.-K. Lau, X. Lu, Y.-J. Hsu, Y. Chen, A.C. Lee, Y. Hou, Y.S. Meng, Q. Li, Revisiting the origin of cycling enhanced capacity of $Fe_3O_4$ based nanostructured electrode for lithium ion batteries, Nano Energy 41 (2017) 426–433, doi:10.1016/j.nanoen.2017.10.001.
[27] Y. Liu, J. Xu, X. Qin, H. Xin, X. Yuan, J. Zhang, D. Li, C. Song, Electrode activation via vesiculation: improved reversible capacity of $\gamma$-$Fe_2O_3$@C/MWNT composite anodes for lithium-ion batteries, J. Mater. Chem. A 3 (18) (2015) 9682–9688, doi:10.1039/C5TA00701A.
[28] K.-H. Kim, W.-S. Kim, S.-H. Hong, Solid solution phosphide ($Mn_{1-x}Fe_xP$) as a tunable conversion/alloying hybrid anode for lithium-ion batteries, Nanoscale 11 (28) (2019) 13494–13501, doi:10.1039/C9NR02016K.
[29] C. Li, A. Sarapulova, K. Pfeifer, S. Dsoke, Effect of continuous capacity rising performed by FeS/$Fe_3C$/C composite electrodes for Lithium-ion batteries, ChemSusChem (2020) 986–995 13(n/a), doi:10.1002/cssc.201903045.
[30] A. Lu, X. Zhang, Y. Chen, Q. Xie, Q. Qi, Y. Ma, D.-L. Peng, Synthesis of $Co_2P$/graphene nanocomposites and their enhanced properties as anode materials for lithium ion batteries, J. Power Sources 295 (2015) 329–335, doi:10.1016/j.jpowsour.2015.06.154.
[31] B. Ravel, M. Newville, ATHENA, ARTEMIS, HEPHAESTUS: data analysis for X-ray absorption spectroscopy using IFEFFIT, J. Synchrotron Rad. 12 (4) (2005) 537–541, doi:10.1107/S0909049505012719.
[32] Y.-M. Lin, P.R. Abel, A. Heller, C.B. Mullins, $\alpha$-$Fe_2O_3$ Nanorods as anode material for lithium ion batteries, J. Phys. Chem. Lett. 2 (22) (2011) 2885–2891, doi:10.1021/jz201363j.
[33] S.J. Hao, B.W. Zhang, S. Ball, J.S. Wu, M. Srinivasan, Y.Z. Huang, Phase transition of hollow-porous alpha-$Fe_2O_3$ microsphere based anodes for lithium ion batteries during high rate cycling, J. Mater. Chem. A 4 (42) (2016) 16569–16575, doi:10.1039/C6TA07131G.
[34] X.P. Lin, J.M. Zhang, X.B. Tong, H. Li, X. Pan, P.G. Ning, Q.H. Li, Templating synthesis of $Fe_2O_3$ hollow spheres modified with Ag nanoparticles as superior anode for lithium ion batteries, Sci. Rep. 7 (2017), doi:10.1038/s41598-017-08773-6.
[35] J.-Y. Shin, D. Samuelis, J. Maier, Sustained lithium-storage performance of hierarchical, nanoporous anatase $TiO_2$ at high rates: emphasis on interfacial storage phenomena, Adv. Funct. Mater. 21 (18) (2011) 3464–3472, doi:10.1002/adfm.201002527.
[36] S. Grugeon, S. Laruelle, L. Dupont, J.M. Tarascon, An update on the reactivity of nanoparticles Co-based compounds towards Li, Solid State Sci. 5 (6) (2003) 895–904, doi:10.1016/S1293-2558(03)00114-6.
[37] Y. Su, B. Fu, G. Yuan, M. Ma, H. Jin, S. Xie, J. Li, Three-dimensional mesoporous $\gamma$-$Fe_2O_3$@carbon nanofiber network as high performance anode material for lithium- and sodium-ion batteries, Nanotechnology 31 (15) (2020) 155401, doi:10.1088/1361-6528/ab6433.
[38] D. Larcher, C. Masquelier, D. Bonnin, Y. Chabre, V. Masson, J.B. Leriche, J.M. Tarascon, Effect of particle size on lithium intercalation into alpha-$Fe_2O_3$, J. Electrochem. Soc. 150 (1) (2003) A133-A139, doi:10.1149/1.1528941.
[39] D. Larcher, D. Bonnin, R. Cortes, I. Rivals, L. Personnaz, J.-M. Tarascon, Combined XRD, EXAFS, and Mössbauer studies of the reduction by lithium of $\alpha$-$Fe_2O_3$ with various particle sizes, J. Electrochem. Soc. 150 (12) (2003) A1643-A1650, doi:10.1149/1.1622959.
[40] X.R. Liu, C.H. Zhao, F. Feng, F.Q. Yu, W.P. Kang, Q. Shen, The controlled synthesis and improved electrochemical cyclability of Mn-doped alpha-$Fe_2O_3$ hollow porous quadrangular prisms as lithium-ion battery anodes, RSC Adv. 5 (10) (2015) 7604–7610, doi:10.1039/C4RA12809E.
[41] M.P. Morales, S. Veintemillas-Verdaguer, C.J. Serna, Magnetic properties of uniform $\gamma$–$Fe_2O_3$ nanoparticles smaller than 5 nm prepared by laser pyrolysis, J. Mater. Res. 14 (7) (2011) 3066–3072, doi:10.1557/JMR.1999.0411.
[42] G. Jain, M. Balasubramanian, J.J. Xu, Structural studies of lithium intercalation in a nanocrystalline alpha-$Fe_2O_3$ compound, Chem. Mater. 18 (2) (2006) 423–434, doi:10.1021/cm052014f.
[43] D. Sneed, J.S.C. Kearney, D. Smith, J.S. Smith, C. Park, A. Salamat, Probing disorder in high-pressure cubic tin (IV) oxide: a combined X-ray diffraction and absorption study, J. Synchrotron Rad. 26 (4) (2019) 1245–1252, doi:10.1107/S1600577519003904.
[44] L. Wang, F. Zhou, Y.S. Meng, G. Ceder, First-principles study of surface properties of $LiFePO_4$: surface energy, structure, Wulff shape, and surface redox potential, Phys. Rev. B 76 (16) (2007) 165435, doi:10.1103/PhysRevB.76.165435.
[45] A.K. Kushwaha, M.R. Sahoo, J. Nanda, S.K. Nayak, Engineering redox potential of lithium clusters for electrode material in lithium-ion batteries, J. Cluster Sci. 28 (5) (2017) 2779–2793, doi:10.1007/s10876-017-1260-7.
[46] D. Mhamane, H.K. Kim, V. Aravindan, K.C. Roh, M. Srinivasan, K.B. Kim, Rusted iron wire waste into high performance anode (alpha-$Fe_2O_3$) for Li-ion batteries: an efficient waste management approach, Green Chem. 18 (5) (2016) 1395–1404, doi:10.1039/C5GC01747E.
[47] Y.-M. Kang, M.-S. Song, J.-H. Kim, H.-S. Kim, M.-S. Park, J.-Y. Lee, H.K. Liu, S.X. Dou, A study on the charge–discharge mechanism of $Co_3O_4$ as an anode for the Li ion secondary battery, Electrochim. Acta 50 (18) (2005) 3667–3673, doi:10.1016/j.electacta.2005.01.012.
[48] J.-C. Liu, X.-L. Ma, Y. Li, Y.-G. Wang, H. Xiao, J. Li, Heterogeneous Fe3 single-cluster catalyst for ammonia synthesis via an associative mechanism, Nat. Commun. 9 (1) (2018) 1610, doi:10.1038/s41467-018-03795-8.